



Title	Formation Mechanism of Microchannels and Lining Layers in Sintered Iron Powder Compacts with Copper Sacrificial Cores
Author(s)	Ohmi, Tatsuya; Kodama, Takuhiro; Iguchi, Manabu
Citation	MATERIALS TRANSACTIONS, 50(12), 2891-2896 https://doi.org/10.2320/matertrans.M2009252
Issue Date	2009-12-01
Doc URL	http://hdl.handle.net/2115/74706
Type	article
File Information	2-2 Formation Mechanism of Microchannels and Lining Layers in Sintered Iron Powder Compacts with Copper Sacrificial Cores.pdf



[Instructions for use](#)

Formation Mechanism of Microchannels and Lining Layers in Sintered Iron Powder Compacts with Copper Sacrificial Cores

Tatsuya Ohmi, Takuhiro Kodama* and Manabu Iguchi

Division of Materials Science and Engineering, Graduate School of Engineering, Hokkaido University, Sapporo 060-8628, Japan

The formation mechanism of microchannels with Fe-Cu alloy lining layers in iron bodies produced by a powder-metallurgical microchanneling process has been investigated. Copper wire was used as a sacrificial core that gives the shape of the microchannel and supplies the alloying element for the lining layer. An iron powder compact containing the sacrificial core was heated and sintered at temperatures between the melting points of copper and iron. Quenching experiments showed that the microchannel was produced just after melting of copper. In a quenched specimen with a newly-formed microchannel, fine copper-rich regions were observed between the iron powder particles in the lining layer. These results established that infiltration of molten copper into the iron powder is the dominant mechanism for the Fe-Cu microchanneling process. It was also found that the liquid copper infiltrated via preferential flow pathways between the iron powder particles.

[doi:10.2320/matertrans.M2009252]

(Received July 21, 2009; Accepted October 8, 2009; Published November 18, 2009)

Keywords: microchannel, microreactor, powder metallurgy, infiltration, diffusion, functional microchannel lining

1. Introduction

Utilization of metallic microreactors for high-temperature reactions has attracted attention in these years. Microreactor technology has possibilities to make a highly-miniaturized system for waste heat utilization and off-gas treatment workable at very short distances from the sources. Such a system could be a prevailing solution for energy saving and greenhouse gas reduction in resources and energy-intensive industries. Metallic materials with good heat conductivity, high-temperature strength and thermal shock resistance are suitable for the microreactor structural material used in this system.

Some practical metals were examined for the microreactor bodies for various reactions in previous reports: stainless steel,¹⁻⁵ FeCrAlloy (Fe-Cr-Al alloy)^{6,7} and aluminum,⁸⁻¹¹ and so on. Guillou *et al.*⁴ reported a stainless steel microreactor for the Fischer-Tropsch synthesis on Co catalyst. Aartun *et al.*⁶ described catalytic conversion of propane to hydrogen in FeCrAlloy microreactors with Ni or Rh catalyst. More recently, Tonkovich *et al.*¹² examined a microreactor with an Inconel 625 body and FeCrAlY-felt catalyst substrate for steam methane reforming with an Rh/MgO/Al₂O₃ catalyst system. FeCrAlloy and FeCrAlY are readily coated with an alumina layer by surface oxidation. Aluminum was also used as the microreactor material because a nanoporous alumina layer produced by anodic oxidation was suitable for a catalyst support. Ganley *et al.*¹⁰ demonstrated the performance of aluminum microreactors with porous alumina layers for the decomposition of anhydrous ammonia.

In most of these previous studies, microchannels were produced by methods of fabricating structured surfaces, for example, mechanical engraving with a fast prototyping machine⁴ or a milling machine,⁵ electrical discharge machining,^{2,10,11} wet-chemical etching,¹ and photoetching.³ The surface-structured workpieces were stacked or sandwiched between the other pieces, and then their matching

surfaces were sealed. Such processes will take extended processing time and much cost.

Recently, we investigated a powder-metallurgical process to produce microchannels directly in metal bodies.¹³⁻¹⁵ Our primary concept for the process was based on a microscopic infiltration phenomenon that often occurs during liquid phase sintering of a mixture of powder metals with different melting points. We used the metal with higher melting point as a body metal, which is to compose the device body, and the other as a sacrificial-core metal, which is to flow out and give the shape of the microchannel. In our experiments, a body-metal powder compact containing a sacrificial core, a shaped sacrificial-core metal, was sintered at temperatures between the melting points of these metals. The molten sacrificial-core metal would migrate to the body-metal powder region by infiltration and partly by diffusion and produce an alloy lining layer surrounding the cavity formed at the site initially occupied by the sacrificial core.

However, our further researches examining various combinations of the metals showed that capability of microchanneling and the structure of lining layers varied depending on the combination.^{16,17} They also suggested that the prepotent mechanism for the migration of the sacrificial-core metal varied from one to another, and in some cases, diffusion acted as the predominant migration mechanism.^{16,17} Figure 1 shows examples of microchanneling behaviors in the specimens with different body metals and a copper sacrificial core: (a) a combination of iron and copper, designated as Fe/Cu, (b) Co/Cu, and (c) Ni/Cu. Clear microchannels and lining layers were produced in the cases of the Fe/Cu and Co/Cu specimens. On the other hand, no microchannel was observed in the Ni/Cu specimen. Possible contributing factors for microchanneling are the wettability and viscosity of the molten sacrificial-core metal, the geometry of the pore space in the body-metal powder compact, the diffusion and reactive properties of these metals, etc. The dominant migration mechanism seems to change depending on these factors, and therefore, on the combination of the metals. However, these factors also

*Graduate Student, Hokkaido University

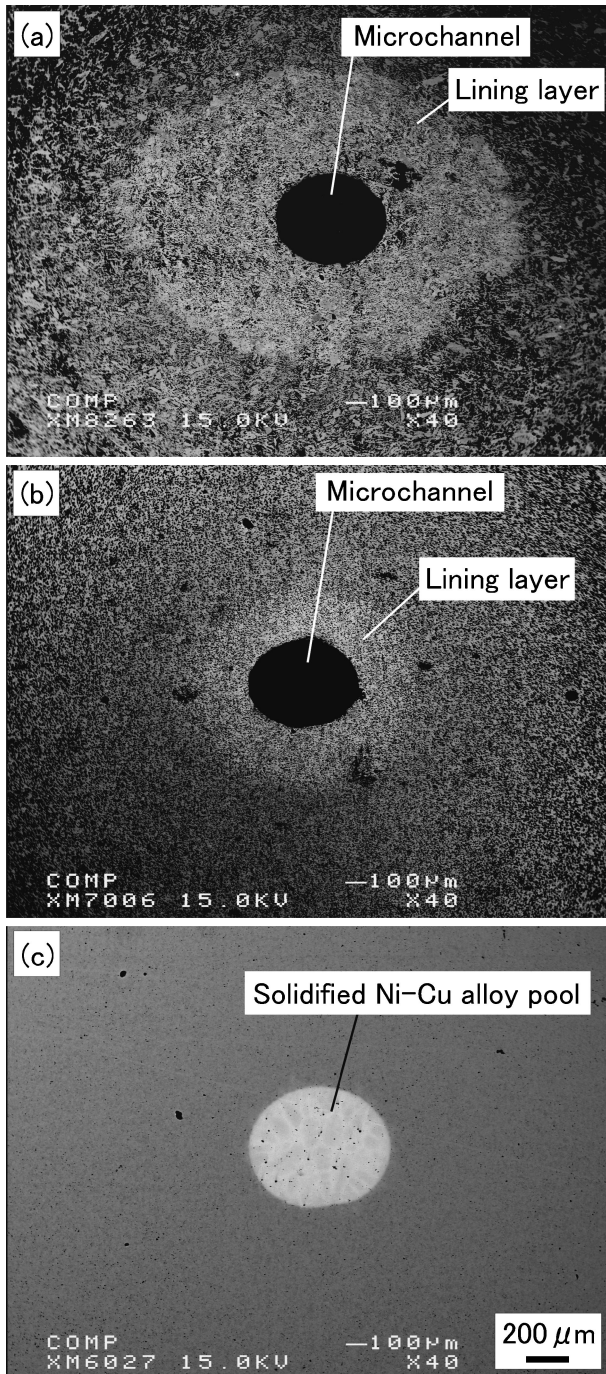


Fig. 1 Back-scattered electron images showing the microchanneling behaviors in the sintered powder compacts of different body metals with a copper sacrificial core: (a) Fe/Cu, (b) Co/Cu, and (c) Ni/Cu.

change during sintering, and the above explanation for the process mechanism still remains a matter of speculation.

In the present study, we investigated the detailed behavior of microchanneling and lining layer formation in Fe/Cu specimens as part of the study to organize the microchanneling mechanism for various metal combinations. It is well known that liquid copper shows extremely good wettability to porous iron substrates.¹⁸⁾ The Fe/Cu combination was, therefore, expected to provide a typical example of an infiltration-dominated microchanneling. It is the reason why this combination was selected as the first one to be investigated.

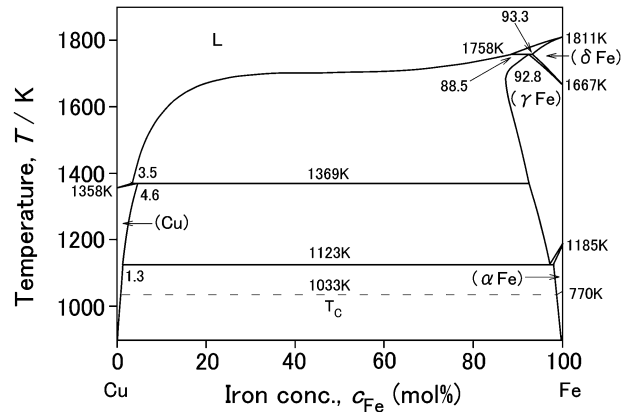


Fig. 2 A Cu-Fe binary alloy phase diagram based on the report by Swartzendruber.¹⁹⁾

2. Experimental Procedure

An iron powder compact containing a copper sacrificial core was sintered in an argon gas atmosphere. The average diameter of the iron powder was 45 μm . The shape of the sacrificial core was a straight wire 500 μm in diameter and 10 millimeters in length. The purity of the iron powder was over 99 mass%, and that of the copper wire was 99.9 mass%. The iron powder with the sacrificial core was cold-pressed into a cylindrical green compact in a stainless steel mold using a unidirectional pressure in the range from 380 to 755 MPa. The resulted green compact had a diameter of 20 mm and nominal height of 5 mm, and its porosity, E , was varied from 22 to 37% depending on the pressing pressure. The initial cross section of the copper wire was round. However, the sacrificial core was distorted into an oblate figure by unidirectional pressing, and the resulted microchannel and lining layer often inherited the shape of the sacrificial core as presented in Fig. 1(a).

We conducted two kinds of sintering experiments: furnace-cooling and quenching experiments. Figure 2 depicts a Cu-Fe binary alloy phase diagram¹⁹⁾ and Fig. 3 illustrates the heating methods used in the experiments. The specimen was set in a vertical furnace in such a way that the sacrificial core was placed horizontally as described in Fig. 3(a). The furnace had a 30 mm inner diameter and a 25 mm-long uniform temperature zone with a uniformity tolerance of ± 2 K. In the furnace-cooling experiments, the green compact specimens were heated at a constant rate of 0.2 K/s from room temperature to 1473 K, and then furnace-cooled at about 0.4 K/s. In the quenching experiments, the specimens were quenched at various temperatures in the course of heating to 1473 K. The maximum temperature, 1473 K, is 115 K higher than the melting point of copper, and within the range of the sintering temperature commonly used in the powder metallurgy of iron and steel.

3. Results and Discussion

3.1 Formation of microchannels

Figure 4(a) and (b) present different cross-sectional structures observed in a specimen quenched at 1358 K, the melting point of copper. They are back-scattered electron

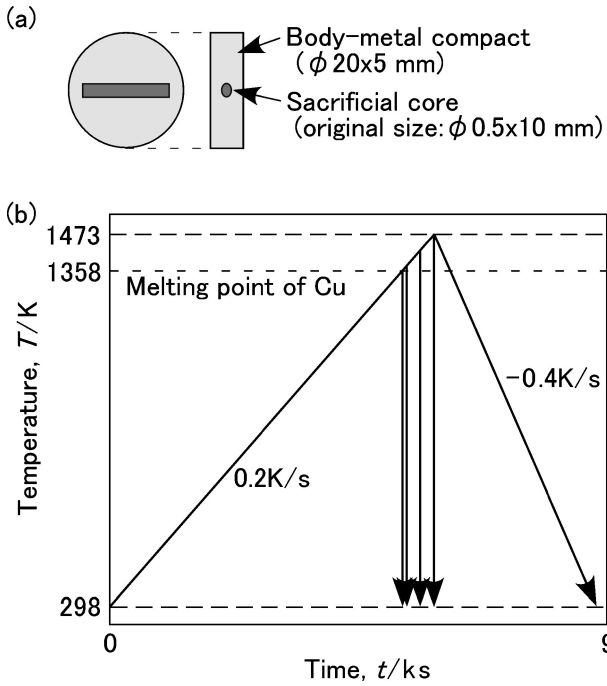


Fig. 3 Sintering procedure. (a) Setting of the specimen in the furnace. (b) Heating and cooling patterns.

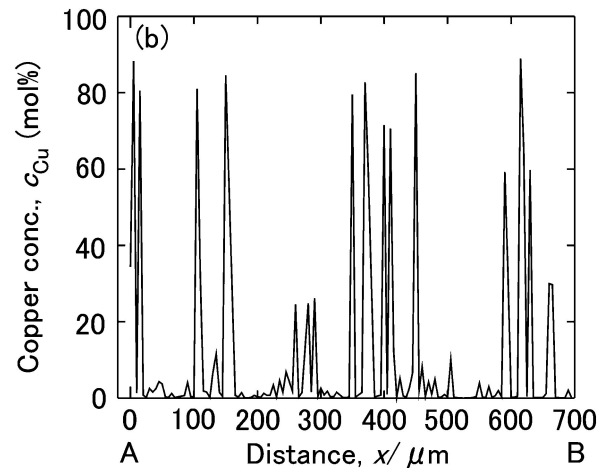
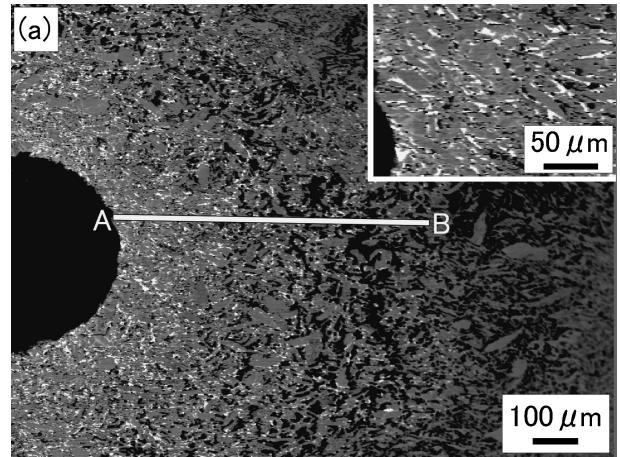


Fig. 5 Back-scattered electron image (a) and copper-concentration profile (b) near the newly-formed microchannel in the specimen quenched at 1363 K. Porosity of the green compact, E , was 36.0%. Diameter of the electron beam and the measurement interval for the EPMA were 1 μm and 5 μm , respectively.

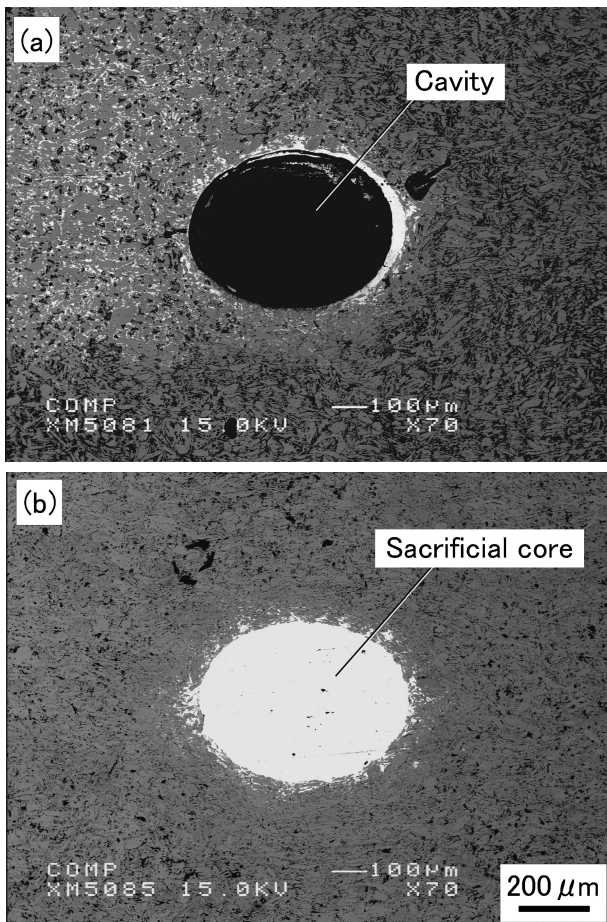


Fig. 4 Back-scattered electron images showing the different cross-sectional structures in a specimen quenched at 1358 K. Porosity of the green compact, E , was 35.0%.

images taken near the sites where the sacrificial core was embedded. The most notable point in these pictures is that a cavity was already forming in Fig. 4(a). This indicates very prompt migration of molten copper. In Fig. 4(b), on the other hand, the sacrificial core still remained at the original site, probably because this portion was solid, or liquid but quenched just before the massive infiltration.

Figure 5(a) contains back-scattered electron images of the lining layer around a newly-formed microchannel. The specimen was quenched at 1363 K, 5 K higher than the melting point of copper. An EPMA line analysis result is provided in Fig. 5(b). The copper-concentration profile in Fig. 5(b) shows many sharp peaks, some of which reached over 80 mol%. Such a copper-rich region can be observed as the white phase in the magnified view of the structure in Fig. 5(a), and shows the infiltration pathway of the molten sacrificial core. However, the copper-concentration was 88.9 mol% at the highest, which is lower than 98.4 mol%, the equilibrium concentration of liquid at 1363 K. This means that the copper-rich phase had already been solidified before quenching, by diffusion of iron from the inner wall of the infiltration pathway, and therefore that the infiltration of the molten sacrificial core had completed in a very short time.

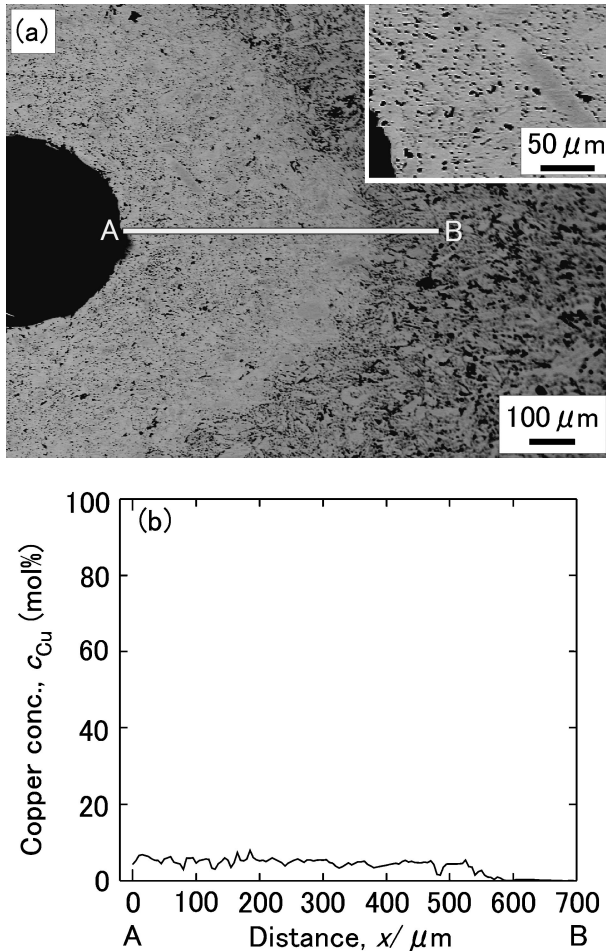


Fig. 6 Back-scattered electron image (a) and copper-concentration profile (b) near the microchannel in the furnace-cooled specimen. Porosity of the green compact, E , was 36.0%. Diameter of the electron beam and the measurement interval for the EPMA were 1 μm and 5 μm , respectively.

The above results clearly show that infiltration is the dominant mechanism of the microchannel formation in the Fe/Cu specimens.

3.2 Structure change of the lining layer during sintering

Figure 6 depicts the structure and copper-concentration profile near the microchannel in the furnace-cooled specimen. The copper-rich spots such as those seen in Fig. 5(a) had already vanished and the concentration profile was smoothed by diffusion. In order to evaluate quantitatively the unevenness of the concentration profile, we now introduce the arithmetical mean deviation of the profile, R_c ;

$$R_c = (1/L) \int_0^L |f(x)| dx \quad (1)$$

where x and L are the distance from the inner wall of the microchannel and the regulation length, respectively. $|f(x)|$ is the absolute difference between the concentration at the position $x = x$, c_x , and the average concentration, c_{av} . The index R_c was diverted from the concept of arithmetical mean roughness described in JIS B 0601(1994) and JIS B 0031(1994). The values of c_{av} and R_c obtained for various specimens are listed in Table 1. R_c decreases monotonously with increasing heating time and/or temperature, therefore

Table 1 Average copper concentration, c_{av} , and arithmetical mean deviation of the concentration profile, R_c . Regulation length, L , was 300 μm . Diameter of the electron beam and the measurement interval for the EPMA were 1 μm and 2 μm , respectively. Porosity of the green compact, E , for each specimen was in the range of 35.5 ± 0.5 (%). The pore regions were omitted from the coverage of calculation.

Specimen	c_{av} (mol%)	R_c (mol%)
Q (1363 K)	9.08	12.76
Q (1373 K)	3.78	4.13
Q (1423 K)	5.14	2.31
Q (1473 K)	6.19	2.13
FC (1473 K)	5.15	1.88

Q: Quenched, FC: Furnace-cooled

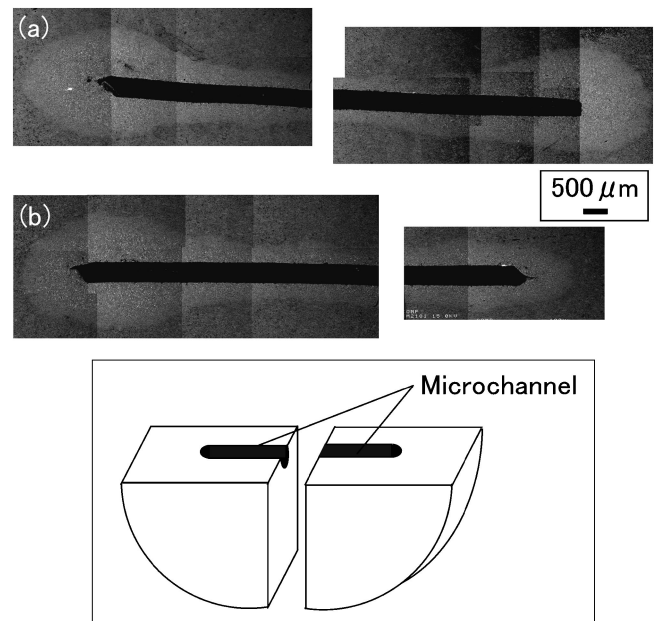


Fig. 7 Structures (back-scattered electron images) of the longitudinal sections through the microchannels produced in the specimens quenched at 1363 K. Porosity of the green compact, E : (a) 28.8%, and (b) 26.2%. The gap in each picture corresponds to the thickness of the cutting blade.

with progression of diffusion. This result successfully demonstrates that the status of homogenization of the copper concentration by diffusion can be quantitatively evaluated by using R_c . On the other hand, c_{av} shows irregular variations, probably because the distribution of the infiltration pathways was not necessarily uniform.

3.3 Evaluation of the volume of the lining layer

In order to get information about the infiltration behavior of the molten sacrificial core, the lining-layer volume, V_L , was estimated metallographically. Figure 7 shows examples of the structures of the longitudinal sections through the microchannels. The specimens were quenched at 1363 K. At this stage, the thickness of the lining layer along the microchannel was not necessarily uniform. This was probably caused by a slight unevenness of the temperature distribution in the specimen and therefore by a time variance of starting infiltration. For example, the lining layer is thickest at the both ends of the microchannel in Fig. 7(a). The cause for this was that the temperature of the inner wall

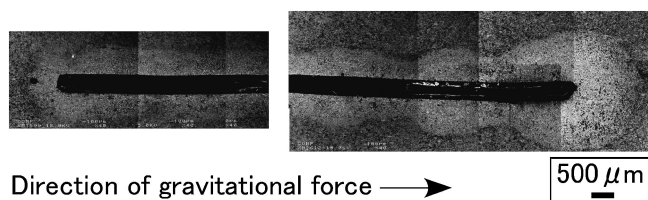


Fig. 8 Structure (back-scattered electron image) of the longitudinal sections through the microchannel produced in the specimen in which the sacrificial core was vertically placed during sintering. The specimen was quenched at 1363 K. Porosity of the green compact, E , was 28.6%. A 13 mm length copper wire was used as the sacrificial core. The gap in the picture corresponds to the thickness of the cutting blade.

of the furnace pipe was higher than inward during sintering. On the other hand, the lining layer is thickest at one end of the microchannel in Fig. 7(b). This was a rare case and probably caused by unintended moving of the specimen from the center axis of the furnace.

In general, there is a possibility that a variation of the hydraulic head pressure across the molten sacrificial core influences the infiltration behavior. Figure 8 presents the result of a comparative experiment using a vertically-placed sacrificial core of 13 mm in length to demonstrate the effects of the hydraulic head pressure on the formation of the lining layer. It was expected that the hydraulic head pressure at the bottom of the microchannel was much higher than that at the top. In Fig. 8, the thickness of the lining layer is clearly larger in the bottom part than in the top part. This result shows that the hydraulic head pressure due to the millimeter-scale vertical interval of up to 13 mm accelerates the infiltration of the molten sacrificial core.

For the case of the horizontally-set sacrificial core, on the other hand, the cross sectional configuration of the lining layer usually shows nearly similar figure as the sacrificial core. This fact indicates that the pressure difference, which was caused by the vertical interval in the range of the major axis length of the cross-sectional configuration of the sacrificial core, did not influence significantly on the infiltration behavior.

Table 2 compares the lining-layer volume, V_L , and the ideal lining-layer volume, V_{Li} , in the specimens with various green-compact porosities, E . All these specimens were quenched at 1363 K. Therefore, the effect of diffusion is negligible. The value of V_L was estimated on the assumption that the lining layer had a similar cross-sectional configuration throughout its length. On the other hand, calculation of V_{Li} was based on the supposition that the lining layer was fully infiltrated and then had no porosity;

$$V_{Li} = V_C/E \quad (2)$$

where V_C is the volume of the microchannel.

It's interesting to note that the values of V_L/V_{Li} in Table 2 are E -independent and are within the range from 4.0 to 5.0. The value of V_L/V_{Li} which is much larger than unity indicates that the molten sacrificial core had infiltrated via preferential flow pathways between the body-metal powder particles.

The V_L/V_{Li} value probably depends on the geometry of the pore-space network with branchings and loops in the

Table 2 Comparison of the microchannel volume, V_C , Lining-layer volume, V_L , and ideal lining-layer volume, V_{Li} , in the specimens with various green-compact porosities, E .

E (%)	$V_C/10^{-9} \text{ m}^3$	$V_L/10^{-9} \text{ m}^3$	$V_{Li}/10^{-9} \text{ m}^3$	V_L/V_{Li}
34.1	1.37	20.26	4.02	5.0
28.8	1.41	19.90	4.90	4.1
26.2	1.35	25.93	5.15	5.0
22.7	1.08	19.20	4.76	4.0

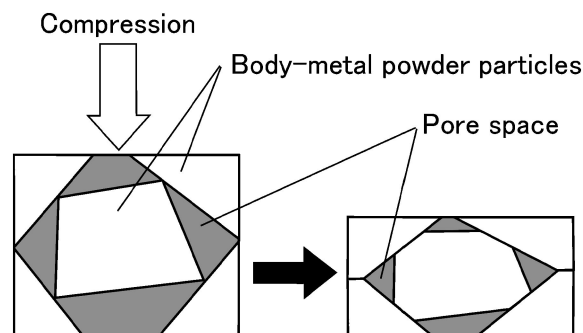


Fig. 9 Schematic illustration of the compression manner of the powder compact keeping the contact points between the powder particles.

compacted powder region. The parameters characterizing the pore-space network, such as the numbers of branchings and loops per unit mass, don't change during compression of the powder compact when the contact points between the powder particles are kept as schematically illustrated in Fig. 9. Considering the fact that the porosity of the close-packed bed with uniform-sized spheres is 26%, the green compacts with porosities from 22.7 to 34.21% might have been prepared in such a manner. At the same time, the parameters depend on the shape and particle size distribution of the body-metal powder. The iron powder used in this study was from the same lot. Therefore, the above discussion may explain the E -independent nature of V_L/V_{Li} shown in Table 2.

The further detailed description of the infiltration behavior from the microscopic aspect is the subject in the future.

4. Conclusions

We investigated the formation mechanism of the microchannels with the alloy lining layers in sintered iron powder compacts containing copper sacrificial cores. The results of our investigation can be summarized as follows.

- (1) The dominant mechanism for the Fe-Cu microchanneling process is infiltration of molten sacrificial core into the body-metal powder. The microchannels are produced just after melting of the sacrificial core.
- (2) The molten sacrificial core infiltrates via preferential flow pathways between the body-metal powder particles.
- (3) The distribution of the sacrificial core metal in the lining layer is homogenized by diffusion during sintering.

REFERENCES

- 1) R. Zapf, C. Becker-Willinger, K. Berresheim, H. Bolz, H. Gnaser, V. Hessel, G. Kolb, P. Löb, A.-K. Pannwitt and A. Ziogas: *Trans. IChemE* **81A** (2003) 721–729.

- 2) Y. S. S. Wan, K. L. Yeung and A. Gavriilidis: *Appl. Catalysis A: General* **281** (2005) 285–293.
- 3) P. V. Snytnikov, M. M. Popova, Y. Men, E. V. Rebrov, G. Kolb, V. Hessel, J. C. Schouten and V. A. Sobyenin: *Appl. Catalysis A: General* **350** (2008) 53–62.
- 4) L. Guillou, S. Paul and V. Le Courtois: *Chem. Eng. J.* **136** (2008) 66–76.
- 5) A. T. Carvalho, R. R. Lima, L. M. Silva, E. W. Simões and M. L. P. Silva: *Sensors Actuators B* **137** (2009) 393–402.
- 6) I. Aartun, T. Gjervan, H. Venvik, O. Görke, P. Pfeifer, M. Fathi, A. Holmen and K. Schubert: *Chem. Eng. J.* **101** (2004) 93–99.
- 7) I. Aartun, B. Silberova, H. Venvik, P. Pfeifer, O. Görke, K. Schubert and A. Holmen: *Catalysis Today* **105** (2005) 469–478.
- 8) E. V. Rebrov, M. H. J. M. de Croon and J. C. Schouten: *Catalysis Today* **69** (2001) 183–192.
- 9) P. Pfeifer, K. Schubert, M. A. Liauw and G. Emig: *Appl. Catalysis A: General* **270** (2004) 165–175.
- 10) J. C. Ganley, K. L. Riechmann, E. G. Seebauer and R. I. Masel: *Journal of Catalysis* **227** (2004) 26–32.
- 11) I. Z. Ismagilov, R. P. Ekatpure, L. T. Tsykoza, E. V. Matus, E. V. Rebrov, M. H. J. M. de Croon, M. A. Kerzhentsev and J. C. Schouten: *Catalysis Today* **105** (2005) 516–528.
- 12) A. L. Y. Tonkovich, B. Yang, S. T. Perry, S. P. Fitzgerald and Y. Wang: *Catalysis Today* **120** (2007) 21–29.
- 13) T. Ohmi, M. Sakurai, K. Matsuura and M. Kudoh: *Proc. 15th Int. Symp. on Transport Phenomena, [(CD-ROM)72]* (2004) 364–367.
- 14) T. Ohmi, K. Matsuura and M. Kudoh: *Int. J. Self-Propag. High-Temp. Synthesis* **13** (2004) 121–129.
- 15) T. Ohmi, M. Takatoo, M. Iguchi, K. Matsuura and M. Kudoh: *Mater. Trans.* **47** (2006) 2137–2142.
- 16) M. Sato, T. Ohmi, M. Iguchi, K. Matsuura and M. Kudoh: *Functionally Graded Materials Vol. 19*, Functionally Graded Material FORUM of JAPAN, (2005) pp. 97–102.
- 17) M. Sato, T. Ohmi, M. Iguchi and K. Matsuura: *Functionally Graded Materials Vol. 20*, Functionally Graded Material FORUM of JAPAN, (2006) pp. 134–139.
- 18) N. Takahira and T. Tanaka: *Netsu Bussei* **20** (2006) 70–74.
- 19) L. J. Swartzendruber: *Phase Diagrams of Binary Iron Alloys*, ed. by H. Okamoto, (ASM International, Materials Park, 1993) pp. 131–137.